BNL-114026-2017-JA

Enhancing CO2 Electroreduction with the Metal-Oxide Interface

D. Gao, Y. Zhang, Z. Zhou, F. Cai, X. Zhao,
W. Huang, Y. Li, J. Zhu, P. Liu, F. Yang, G. Wang, X. Bao

Submitted to Journal of the American Chemical Society

April 2017

Chemistry Department

Brookhaven National Laboratory

U.S. Department of Energy
USDOE Office of Science (SC),
Basic Energy Sciences (BES) (SC-22)

DISCLAIMER

Enhancing CO_2 Electroreduction with the Metal-Oxide Interface

Dunfeng Gao,[‡a] Yi Zhang,[‡a, b] Zhiwen Zhou, [‡a, b] Fan Cai, [a, b] Xinfei Zhao, [a, b] Wugen Huang,[a, b] Yangsheng Li,[a, b] Junfa Zhu,[c] Ping Liu,[d] Fan Yang,*[, a] Guoxiong Wang,*[, a] Xinhe Bao*[, a]

[a]State Key Laboratory of Catalysis, CAS Center for Excellence in Nanoscience, Dalian National Laboratory for Clean Energy, Dalian Institute of Chemical Physics, Chinese Academy of Sciences, Dalian, 116023, China

[b]University of Chinese Academy of Sciences, Beijing, 100039, China

[c]National Synchrotron Radiation Laboratory, Collaborative Innovation Center of Suzhou Nano Science and Technology, University of Science and Technology of China, Hefei, 230029, China

[d]Chemistry Department, Brookhaven National Laboratory, Upton, New York 11973, United States

Supporting Information Placeholder

ABSTRACT: The electrocatalytic reduction of CO_2 is a promising process to achieve efficient carbon cycle and renewable electricity storage. As the process typically used transition metals as the catalysts, tremendous efforts have been dedicated to improve the efficiency of CO_2 electroreduction by tuning the morphology, size and structure of these metal catalysts and by employing electrolytes that could enhance the adsorption of CO_2. We report here a strategy by constructing the metal-oxide interface to enhance CO_2 electroreduction and demonstrate that Au-CeO_x shows much higher activity and Faradaic efficiency than Au or CeO_x alone for CO_2 electroreduction. In situ scanning tunnelling microscopy and synchrotron-radiation photoemission spectroscopy show that the Au-CeO_x interface is dominant in enhancing CO_2 adsorption and activation, which can be further promoted by the presence of hydroxyl groups. Density functional theory calculations also indicate that the Au-CeO_x interface is the active site for CO_2 activation and the reduction to CO, where the synergy between Au and CeO_x promotes the stability of key carboxyl intermediate (*COOH) and subsequently the conversion of CO_2. Similar interface-enhanced CO_2 electroreduction is further observed at the Ag-CeO_x interface, demonstrating the generality of the strategy for enhancing CO_2 electroreduction.

Electrocatalytic reduction of CO_2 is considered as a potential approach to convert CO_2 to fuel and chemicals powered by renewable electricity[1]. However, the process has been hampered by the large overpotential in reducing CO_2, which leads to a sharp decrease in product selectivity and energy efficiency[1,2]. The initiation of CO_2 electroreduction by transferring one electron to the linear CO_2 molecule and forming a bent CO_2^- intermediate, requires a very negative potential of –1.9 V vs. standard hydrogen electrode (SHE)[3]. With electrocatalysts, this potential can be positively shifted via the enhanced CO_2 chemisorption and the stabilization of reaction intermediates[1]. Over the past years, tremendous efforts have been dedicated to develop and improve the performance of metal catalysts for CO_2 electroreduction[4,5], among which controlling the size, shape and morphology of nanostructured metal catalysts has been shown as an effective strategy[5]. Meanwhile, the use of metal catalysts for CO_2 electroreduction faces a major problem in the very weak adsorption of CO_2 on transition metal surfaces[6]. To enhance the solubility and adsorption of CO_2, ionic liquid electrolytes[7], nitrogen-containing organic molecules[8] and polymers[9] have been employed as sorbents or co-catalysts. These methods, however, suffer a few drawbacks, such as expensive, complicated catalyst preparation procedures and difficulty in liquid product separation.

To address the above issues, we propose a strategy to facilitate CO_2 electroreduction through the construction of the metal-oxide interface. The remarkable catalytic properties of the metal-oxide interface have been increasingly recognized in heterogeneous catalytic processes, such as CO oxidation[10], water-gas shift reaction[11] and methanol synthesis[12]. The strong interfacial interaction, particularly the interface confinement effect in supported nanostructures, has been suggested to provide and stabilize highly active sites for molecular activation[13]. Such interfacial interaction or catalytic chemistry has rarely been noticed or utilized for electrocatalysis, especially for CO_2 electroreduction. In this study, we show that the construction of metal-oxide interfaces could indeed introduce catalytic properties, much different from those of metals or oxides alone. Taking Au and Ag catalysts as an example, though these catalysts have been exploited as potential candidates for CO_2 electroreduction[14], they suffer the problems of large overpotential and low Faradaic efficiency[4]. Our study show that the activation of CO_2 and the subsequent hydrogenation reactions could be significantly enhanced by the metal-CeO_x interface, which provides a new route for the design of efficient catalysts for CO_2 electroreduction, and for electrocatalysis in general.

CO_2 electroreduction was studied over Au/C, CeO_x/C and Au-CeO_x/C catalysts under the same reaction conditions. The sizes of Au nanoparticles (NPs) were controlled in the Au/C and Au-CeO_x/C catalysts to show a similar size distribution and average size, as confirmed by X-ray diffraction (XRD, Figure S1) and transmission electron microscopy (TEM, Figure S2). The average size of these supported Au

NPs is around 7 nm, which has been shown previously as the optimum size for CO_2 electroreduction[15]. The grain size of ceria NPs is approximately 10.5 nm, as calculated from XRD spectra. The actual metal loadings of Au/C, CeO_x/C and Au-CeO_x/C catalysts were determined by inductively coupled plasma optical emission spectroscopy (ICP-OES) and listed in Table S1. Figure 1a shows, in Au-CeO_x/C catalyst, Au NPs sit on CeO_x NPs, forming Au-CeO_x interfaces. The lattice distances of Au and CeO_x NPs are 0.24 and 0.31 nm, corresponding to those of Au(111) and CeO_2 (111), respectively. X-ray photoelectron spectroscopy (XPS) also confirms that Au NPs in Au-CeO_x/C and Au/C catalysts remain the metallic state (Figures S3). Meanwhile, Ce 3d XPS spectra show the mixture of Ce^{4+} and Ce^{3+} in both Au-CeO_x/C (Figure S3b) and CeO_x/C (Figure S3d) catalysts. The atomic fraction of Ce^{3+}, obtained by fitting the Ce $3d_{5/2}$ peaks[16], increases from 21.6% in CeO_x/C to 30.9% in Au-CeO_x/C (Table S1). The increase in Ce^{3+} concentration is not influenced by the reducing agent during synthesis (Figures S3), but rather induced by the strong interfacial interaction between Au and ceria, which facilitates the removal/desorption of lattice oxygen and thus the reduction of CeO_x[17,18].

The reactivity of the above catalysts for CO_2 electroreduction was measured in an H-cell (separated by Nafion 115) filled with 0.1 M $KHCO_3$ (pH 6.8) solution[19]. Under the reported reaction conditions, CO and H_2 are the only two gas products, and no liquid products are detected by nuclear magnetic resonance (NMR). The CO Faradaic efficiency reaches ~89% over Au-CeO_x/C at −0.89 V vs. reversible hydrogen electrode (RHE), which are significantly higher than 58.9% and 9.4% over Au/C and CeO_x/C at the same potential (Figure 1b). The geometric current density for CO production over Au-CeO_x/C (13.1 mA cm^{-2}) is about 1.6 times higher than that over Au/C (8.1 mA cm^{-2}) at −0.89 V vs. RHE (Figure 1c). An appreciable amount of CO (0.59 mA cm^{-2}) is produced at −0.49 V vs. RHE over Au-CeO_x/C, which is 0.38 V below the theoretical equilibrium potential (−0.11 V vs. RHE). The onset potential of CO_2 electroreduction shifts positively by ~ 0.1 V over Au-CeO_x/C, when compared with Au/C. Figure S4a shows the mass activity reaches 32.7 A g^{-1}_{Au} at −0.89 V vs. RHE over Au-CeO_x/C, which is 1.6 times higher than that over Au/C (20.3 A g^{-1}_{Au}), and 3.3 times higher than that on 6 or 8 nm Au NPs (~9.8 A g^{-1}_{Au}) reported previously[15]. In terms of the specific activity by normalizing the current for CO production with electrochemical surface area (ECSA)[20], Au-CeO_x/C exhibits an intrinsic activity ~ 2.3 times higher than that of Au/C in the whole potential range (Figure 1d), while the ESCA of Au-CeO_x/C, 9.57 m^2 g^{-1}_{Au}, is lower than that of Au/C, 13.32 m^2 g^{-1}_{Au} (Figure S5). On the other hand, although CeO_x/C shows an appreciable capacity for CO_2 adsorption, current densities for CO production are almost equal over CeO_x/C and Vulcan XC-72R (Figure 1c), suggesting that CeO_x cannot reduce CO_2 to CO by itself.

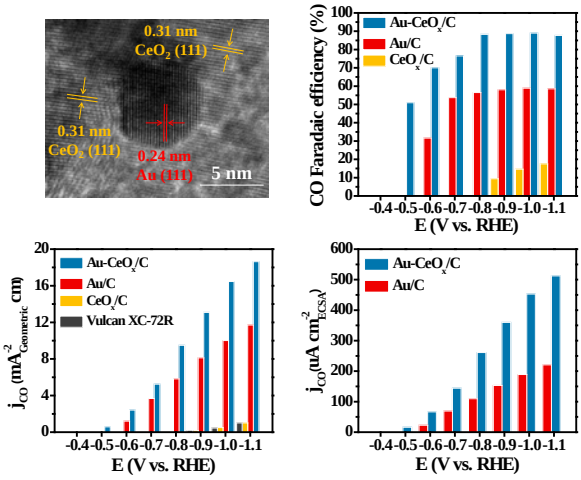

Figure 1. Structure and performance of Au-CeO_x/C catalyst. (a) HRTEM image of Au-CeO_x catalyst. (b) Faradaic efficiency, (c) geometric partial current density, and (d) specific activity for CO production over Au/C, CeO_x/C and Au-CeO_x/C in CO_2-saturated 0.1 M $KHCO_3$ solution and their dependence on the applied potentials. Current density for CO production over Vulcan XC-72R is also shown in (c).

To understand the role of the Au-CeO_x interface in enhancing CO_2 electroreduction, we constructed CeO_x islands on Au(111) to study the interaction between the Au-CeO_x interface and CO_2/H_2O. Depending on the surface coverage, CeO_x islands on Au(111) could display a range of thickness, from monolayer to multilayer (Figure S6). Each layer of CeO_x islands consists of an O-Ce-O trilayer and exhibits the fluorite structure of CeO_2(111), as depicted by the atomic scanning tunnelling microscopy (STM) images in Figure 2. The step edges of CeO_x islands expose exclusively undercoordinated Ce^{3+} ions, rendering a higher apparent height of step edges in STM (Figure 2b). When the CeO_x/Au(111) surface was exposed to CO_2 at 78 K, CO_2 was found to adsorb and enrich at the CeO_x-Au(111) interface. In situ STM images (Figures 2c and 2d) clearly show the addition of an extra row of adsorbates along the step edge of ceria. At this stage, no adsorption of CO_2 was observed on the surface of CeO_x, even with the presence of surface oxygen vacancy sites (Figure 2c). Upon further CO_2 exposure, adsorbates start to appear on the surface of CeO_x, but only at the vicinity of prior adsorbed species (Figures 2e, and S7), forming an adsorbate ring around the periphery of the CeO_x island. As CO_2 adsorption continues, adsorbates propagate towards the center of the CeO_x island until the whole surface is covered by CO_2 (Figure 2f). Yet, no adsorption of CO_2 was found on Au(111) upon extended CO_2 exposure. In comparison, CO_2 adsorption on the CeO_2(111) film occurs primarily at the step edges and surface defects at 78 K (Figure S8), whereas CO_2 on flat terraces appears diffusive, indicating a weak physisorption and consistent with previous report[21]. The chemical nature of adsorbed species was probed by synchrotron-radiation photoemission spectroscopy (SRPES), which gave a C 1s peak at 289.7 eV and suggested the formation of $CO_2^{\delta-}$ species on ceria and at the CeO_x-Au(111) interface[22]. SRPES and STM results also show that the adsorbed $CO_2^{\delta-}$ species started to desorb at 200 K and desorbed mostly when annealed to 300 K in UHV (Figure 3a).

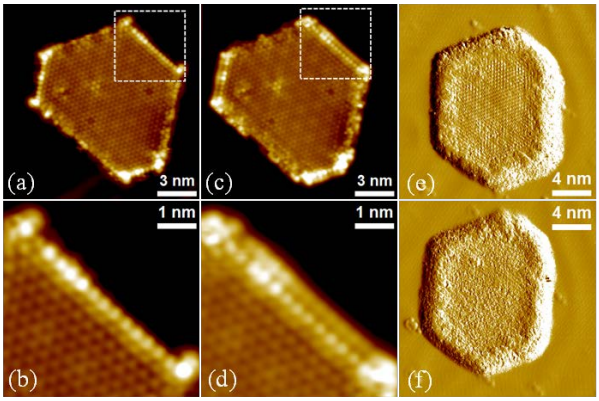

Figure 2. The interaction between CeO_x/Au(111) and CO_2. (a-d) STM images of the CeO_x-Au(111) interface before (a, b) and after (c, d) CO_2 adsorption at 78 K. The CeO_x island displays the atomic structure of CeO_2(111). (b) and (d) are the magnified STM images of the areas shown in (a) and (c), respectively. (e-f) Sequential STM images of the CeO_x island upon extended CO_2 exposure at 78 K. CO_2 adsorbates propagate from the interface to the surface of CeO_x, until the entire ceria terrace is covered with CO_2. Scanning parameters: (a, c) V_s = 600 mV; I_t = 0.2 nA. (b, d) V_s = 260 mV; I_t = 0.15 nA.

Our results thus reveal a unique capability of the CeO_x-Au(111) interface in not only activating CO_2, but also facilitating the subsequent adsorption of CO_2 on ceria. Conventionally, one would assume a random adsorption model in the surface reaction of chemical molecules. Our results clearly demonstrated that the CeO_x-Au interface enables a new pathway, where previously activated CO_2 species serve as the active sites, facilitating and drastically enhancing the subsequent activation of CO_2. As such, the interfacial effect is no longer local, but a global effect. Accordingly, temperature programmed desorption (TPD) studies of CO_2 adsorption over the powder catalysts (Figure S9) show that Au/C only produced a very weak CO_2 desorption peak[6], whereas Au-CeO_x/C showed a desorption peak area, much larger than the sum of the desorption peaks from Au/C and CeO_x/C.

The influence of water is essential to CO_2 electroreduction. Senanayake et al.[23] have reported that water dissociates spontaneously, producing hydroxyl groups, upon its adsorption at the CeO_x-Au(111) interface at 100 K, which is also confirmed in our SRPES measurements (Figure S12, S13c). Upon annealing, water molecules would desorb below 300 K, whereas OH groups were stable up to 500 K[23]. On this basis, we studied the interaction between CO_2 and the hydroxylated CeO_x/Au(111), and found that OH groups could facilitate the adsorption and activation of CO_2. Figure 3a shows, in the absence of H_2O, $CO_2^{\delta-}$ species would desorb from CeO_x/Au(111) after the annealing to 300 K. With the co-deposition of H_2O, more $CO_2^{\delta-}$ species were found on CeO_x/Au(111), and could be stabilized when H_2O and CO_2 were dosed together at 300 K (Figure 3a and S11c). Accordingly, STM results also show the formation of surface adsorbates at the surface of CeO_x islands at 300 K, which was not observed when only CO_2 was dosed (Figure S10).

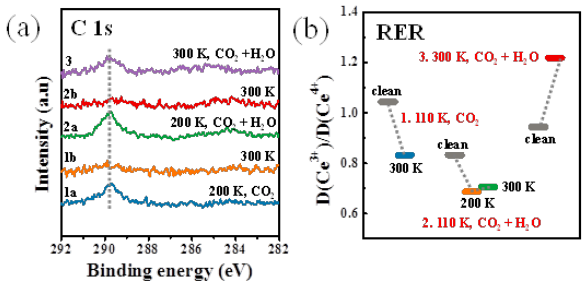

Figure 3. The interaction between CeO_x/Au(111) and CO_2/H_2O. (a) C 1s spectra (hν= 400 eV) of CeO_x/Au(111) taken after the exposure of CO_2 and H_2O. (1a: the exposure to 15 L CO_2 at 150 K and annealing to 200 K, 1b: the subsequent annealing to 300 K. 2a: the exposure to 15 L CO_2 and 3 L H_2O at 110 K and annealing to 200 K, 2b: the subsequent annealing to 300 K. 3: the co-exposure to 500 L CO_2 and 50 L H_2O at 300 K). The major peak at 289.7 eV has been assigned as $CO_2^{\delta-}$ species[22]. (b) The corresponding density ratios of $D(Ce^{3+})/D(Ce^{4+})$, as calculated from the intensity of RPES spectra of Ce^{3+} and Ce^{4+}, and termed as resonant enhancement ratio (RER). The changes in oxidation states of CeO_x are compared before and after the treatments.

From the resonant photoemission spectroscopy (RPES) of CeO_x/Au(111) (see Supporting Information for details), we observed an increased reduction of CeO_x, accompanying the enhanced formation and stabilization of $CO_2^{\delta-}$ species (Figure 3b). As for the interaction of ceria with H_2O or CO_2 alone, we found the adsorption of CO_2 caused the oxidation of ceria, whereas OH groups facilitated the reduction of ceria to produce surface Ce^{3+} sites (Figure S13). Indeed, the reduction of CeO_x islands in water vapour is more drastic than annealing in UHV or in a CO environment (Figure S13d), consistent with previous reports on the reduction of CeO_{2-x} by water at 300 K[24,25], or elevated temperatures[26]. The facilitated reduction of CeO_x in H_2O has been attributed to the H_2O/OH promoted redistribution of oxygen vacancies from bulk to surface, by stabilizing Ce^{3+} sites at the surface[26]. In our case, the facile dissociation of water at interfacial Ce^{3+} sites promotes the formation of surface hydroxyl groups, which subsequently facilitates the removal of lattice oxygen upon annealing. By enhancing the reduction of CeO_x to form high concentration of Ce^{3+} sites, the presence of water also improves the adsorption and stability of $CO_2^{\delta-}$ species on CeO_x/Au(111).

The activation of CO_2 and the stabilization of $CO_2^{\delta-}$ species enable the subsequent hydrogenation process. To gain better understanding of the reaction mechanism, we conducted density functional theory (DFT) calculations using Ce_3O_7/Au(111) to describe the Au-CeO_x interface. In addition, the full hydroxylation of Ce_3O_7 to $Ce_3O_7H_7$ was included to account for the effect of electrochemical environment for CO_2 reduction[27]. Following previous studies on CO_2 electroreduction to CO, we considered the following reaction mechanism[28,29]:

$$CO_2(g) + * + H^+(aq) + e^- \rightarrow *COOH \quad (1)$$

$$*COOH + H^+(aq) + e^- \rightarrow *CO + H_2O(l) \quad (2)$$

$$*CO \rightarrow CO(g) + * \quad (3)$$

Figure 4 shows the calculated free energy diagram for the electrochemical reduction from CO_2 to CO on $Ce_3O_7H_7$/Au(111) . The formation of carboxyl (*COOH) species via protonation (1) is found as the potential limiting step on both $Ce_3O_7H_7$/Au(111) and Au(111), while the corresponding energy cost on $Ce_3O_7H_7$ /Au(111) is 0.33 eV lower than that on Au(111). By comparison, the sequential protonated decomposition of *COOH to *CO (2) and the removal of *CO (3) desorption are more favourable. Accordingly, the CeO_x-Au interface is able to enhance CO_2 electroreduction, in agreement with our experimental observations.

To understand the active site in CeO_x, we also performed a Bader charge analysis. For Ce_3O_7/Au(111), the oxidation state of Ce in the cluster is +3.60 (See Supporting information for details), which is lower than that in Ce_3O_7 alone. The hydroxylation to $Ce_3O_7H_7$/Au(111) further decreases the oxidation state of Ce to +3.28. That is, the strong interaction with Au and the hydroxylation result in the reduction of Ce ions. Figure 4 shows that the key *COOH intermediate is stabilized by reduced Ce site at the interface, via the direct interaction with one of terminal oxygen and thus enhance the overall electrochemical reduction of CO_2.

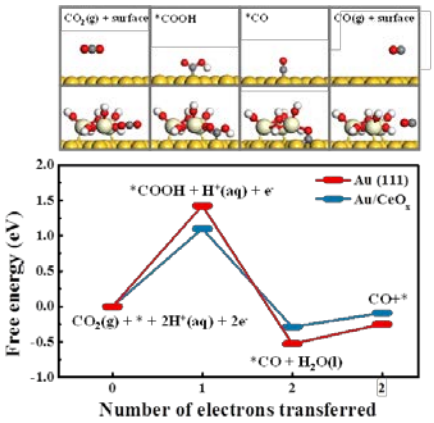

Figure 4. Calculated free energy diagram for CO_2 electroreduction to CO at 0 V vs. RHE on $Ce_3O_7H_7$/Au(111) and Au(111). "*" indicates a free surface site. The optimized structures for the main intermediates are shown above the figure. Colors: O (red), C (gray), H (white), cerium (light-beige), gold (golden yellow).

Having understood the catalytic nature of CO_2 electroreduction at the Au-CeO_x interface, we realize that these insights might enable us to improve further the catalytic performance of other metals by interface enhancement. We have thus synthesized Ag-CeO_x/C catalyst (Figure S14) and compared its performance in CO_2 electroreduction with Ag/C catalyst. Similar to the behavior of Au-CeO_x/C catalyst, CO_2 electroreduction over the Ag-CeO_x/C catalyst produces only CO and H_2, and no liquid products are detected by NMR. Faradaic efficiency for CO production over Ag-CeO_x/C has reached 92.6% at –0.89 V vs. RHE, much higher than 56.6% over Ag/C at the same potential (Figure S15a). The partial current density (Figure S15b) and mass activity (Figure S4b) for CO production at Ag-CeO_x/C are also significantly higher than those over Ag/C in the whole potential range. Compared with Ag/C catalyst, Ag-CeO_x/C catalyst could enhance the production of CO by over a magnitude at –0.69 V vs. RHE or lower potentials. Ag-CeO_x/C catalyst also shifts the onset potential of CO_2 electroreduction by ~ 0.2 V positively with respect to the overpotential over Ag/C. Therefore, enhanced CO_2 electroreduction is further verified at the Ag-CeO_x interface.

In summary, we demonstrate that the construction of the metal-oxide interface could significantly enhance the activity and selectivity of CO_2 electroreduction. Au-CeO_x/C catalyst shows a geometric current density 1.6 times higher than that of the optimum Au/C catalyst at –0.89 V vs. RHE, which leads to a Faradaic efficiency of ~89% for CO production. The enhancement is attributed to the drastically enhanced CO_2 adsorption and activation by the Au-CeO_x interface, which can not only activate CO_2 at interfacial sites, but also facilitate the subsequent adsorption of CO_2 on ceria terraces. Further, OH groups from water dissociation enhance the reduction of CeO_x and the stability of $CO_2^{\delta-}$ species. The subsequent formation of carboxyl species (*COOH), i.e. the potential limiting step, gives a free energy 0.33 eV lower at the CeO_x/Au(111) interface than on Au(111). Thus, by strengthening the adsorption of *COOH at the interface, CO_2 electroreduction is greatly facilitated. Interface-enhanced CO_2 electroreduction was also observed on the Ag-CeO_x catalyst, which displays a geometric current density over 3 times higher than that of the Ag/C catalyst at –0.89 V vs. RHE and a Faradaic efficiency of 92.6% for CO production. Therefore, our study demonstrates the unique catalytic properties of the metal-oxide interface in enhancing CO_2 electroreduction and provides a new route for the design of efficient electrocatalysts.

ASSOCIATED CONTENT

Supporting Information

Details of experimental procedures, data analysis and DFT calculations. This material is available free of charge via the Internet at http://pubs.acs.org.

AUTHOR INFORMATION

Corresponding Author

fyang@dicp.ac.cn
wanggx@dicp.ac.cn
xhbao@dicp.ac.cn

Author Contributions

‡These authors contributed equally.

Notes

The authors declare no competing financial interests.

ACKNOWLEDGMENT

This work was financially supported by Natural Science Foundation of China (21573222, 21473191, 21303195) and Strategic Priority Research Program of the Chinese Academy of Sciences (XDB17020200). P. L. would like to thank the support from the US Department of Energy, Division of Chemical Sciences under contract DE-SC0012704. We thank Dr. Huanxin Ju, Dr. Shanwei Hu and Dr. Qian Xu from the BL11U beamline in NSRL for assistance with SRPES measurements. G.X. Wang also thanks the financial support from CAS Youth Innovation Promotion.

REFERENCES

(1) Whipple, D. T.; Kenis, P. J. A., *J. Phys. Chem. Lett.* **2010**, *1*, 3451.
(2) Kortlever, R.; Shen, J.; Schouten, K. J. P.; Calle-Vallejo, F.; Koper, M. T. M., *J. Phys. Chem. Lett.* **2015**, *6*, 4073.
(3) Schwarz, H. A.; Dodson, R. W., *J. Phys. Chem.* **1989**, *93*, 409.
(4) Hori, Y. *In Modern Aspects of Electrochemistry*; Vayenas, C. G., Ed.; Springer: New York, 2008; p 89.
(5) Gao, D.; Cai, F.; Wang, G.; Bao, X., *Curr. Opin. Green Sustainable Chem.* **2017**, *3*, 39.
(6) Freund, H. J.; Roberts, M. W., *Surf. Sci. Rep.* **1996**, *25*, 225.
(7) Rosen, B. A.; Salehi-Khojin, A.; Thorson, M. R.; Zhu, W.; Whipple, D. T.; Kenis, P. J. A.; Masel, R. I., *Science* **2011**, *334*, 643.
(8) Cao, Z.; Kim, D.; Hong, D. C.; Yu, Y.; Xu, J.; Lin, S.; Wen, X. D.; Nichols, E. M.; Jeong, K.; Reimer, J. A.; Yang, P. D.; Chang, C. J., *J. Am. Chem. Soc.* **2016**, *138*, 8120.
(9) Li, F.; Zhao, S. F.; Chen, L.; Khan, A.; MacFarlane, D. R.; Zhang, J., *Energy Environ. Sci.* **2016**, *9*, 216.
(10) Fu, Q.; Li, W. X.; Yao, Y. X.; Liu, H. Y.; Su, H. Y.; Ma, D.; Gu, X. K.; Chen, L. M.; Wang, Z.; Zhang, H.; Wang, B.; Bao, X. H., *Science* **2010**, *328*, 1141.
(11) Rodriguez, J. A.; Ma, S.; Liu, P.; Hrbek, J.; Evans, J.; Perez, M., *Science* **2007**, *318*, 1757.
(12) Graciani, J.; Mudiyanselage, K.; Xu, F.; Baber, A. E.; Evans, J.; Senanayake, S. D.; Stacchiola, D. J.; Liu, P.; Hrbek, J.; Sanz, J. F.; Rodriguez, J. A., *Science* **2014**, *345*, 546.
(13) Yang, F.; Deng, D. H.; Pan, X. L.; Fu, Q.; Bao, X. H., *Natl. Sci. Rev.* **2015**, *2*, 183.
(14) Back, S.; Yeom, M. S.; Jung, Y., *ACS Catal.* **2015**, *5*, 5089.
(15) Zhu, W. L.; Michalsky, R.; Metin, O.; Lv, H. F.; Guo, S. J.; Wright, C. J.; Sun, X. L.; Peterson, A. A.; Sun, S. H., *J. Am. Chem. Soc.* **2013**, *135*, 16833.
(16) Bu, Y.; Weststrate, C. J.; Niemantsverdriet, J. W.; Fredriksson, H. O. A., *ACS Catal.* **2016**, 7994.
(17) Vayssilov, G. N.; Lykhach, Y.; Migani, A.; Staudt, T.; Petrova, G. P.; Tsud, N.; Skála, T.; Bruix, A.; Illas, F.; Prince, K. C.; Matolı´n, V. Â. r.; Neyman, K. M.; Libuda, J. r., *Nat. Mater.* **2011**, *10*, 310-315.
(18) Mullins, D. R., *Surf. Sci. Rep.* **2015**, *70*, 42.
(19) Gao, D. F.; Zhou, H.; Wang, J.; Miao, S.; Yang, F.; Wang, G. X.; Wang, J. G.; Bao, X. H., *J. Am. Chem. Soc.* **2015**, *137*, 4288.
(20) Hebie, S.; Holade, Y.; Maximova, K.; Sentis, M.; Delaporte, P.; Kokoh, K. B.; Napporn, T. W.; Kabashin, A. V., *ACS Catal.* **2015**, 5, 6489.
(21) Senanayake, S. D.; Mullins, D. R., *J. Phys. Chem. C* **2008**, *112*, 9744.
(22) Senanayake, S. D.; Ramirez, P. J.; Waluyo, I.; Kundu, S.; Mudiyanselage, K.; Liu, Z.; Liu, Z.; Axnanda, S.; Stacchiola, D. J.; Evans, J., *J. Phys. Chem. C* **2016**, *120*, 1778.
(23) Senanayake, S. D.; Stacchiola, D.; Evans, J.; Estrella, M.; Barrio, L.; Perez, M.; Hrbek, J.; Rodriguez, J. A., *J. Catal.* **2010**, *271*, 392.
(24) Lykhach, Y.; Johanek, V.; Aleksandrov, H. A.; Kozlov, S. M.; Happel, M.; Skala, T.; St Petkov, P.; Tsud, N.; Vayssilov, G. N.; Prince, K. C.; Neyman, K. M.; Matolin, V.; Libuda, J., *J. Phys. Chem. C* **2012**, *116*, 12103.
(25) Berner, U.; Schierbaum, K.; Jones, G.; Wincott, P.; Haq, S.; Thornton, G., *Surf. Sci.* **2000**, *467*, 201.
(26) Henderson, M. A.; Perkins, C.; Engelhard, M. H.; Thevuthasan, S.; Peden, C. H., *Surf. Sci* **2003**, *526*, 1.
(27) Zhao, X.; Ma, S.; Hrbek, J.; Rodriguez, J. A., *Surf. Sci.* **2007**, *601*, 2445.
(28) Peterson, A. A.; Abild-Pedersen, F.; Studt, F.; Rossmeisl, J.; Norskov, J. K., *Energy Environ. Sci.* **2010**, *3*, 1311.
(29) Hansen, H. A.; Varley, J. B.; Peterson, A. A.; Norskov, J. K., *J. Phys. Chem. Lett.* **2013**, *4*, 388.

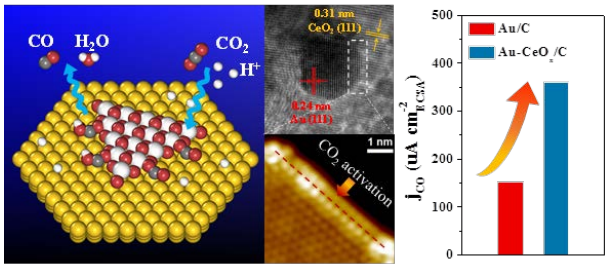

Insert Table of Contents artwork here